

Disentangled 4D Gaussian Splatting: Towards Faster and More Efficient Dynamic Scene Rendering

Hao Feng¹ Hao Sun¹ Wei Xie^{1*}
¹Central China Normal University



Figure 1. We present Disentangled 4D Gaussian Splatting, a novel approach that takes videos as input and synthesizes dynamic novel-view images with fine details. The proposed method surpasses previous approaches in both rendering quality and speed, achieving an inference speed of 343 FPS on an RTX 3090 in the Plenoptic Dataset[14].

Abstract

Novel-view synthesis (NVS) for dynamic scenes from 2D images presents significant challenges due to the spatial complexity and temporal variability of such scenes. Recently, inspired by the remarkable success of NVS using 3D Gaussian Splatting (3DGS), researchers have sought to extend 3D Gaussian models to four dimensions (4D) for dynamic novel-view synthesis. However, methods based on 4D rotation and scaling introduce spatiotemporal deformation into the 4D covariance matrix, necessitating the slicing of 4D Gaussians into 3D Gaussians. This process increases redundant computations as timestamps change—an inherent characteristic of dynamic scene rendering. Additionally, performing calculations on a four-dimensional matrix is computationally intensive. In this paper, we introduce **Disentangled 4D Gaussian Splatting (Disentangled4DGS)**, a novel representation and rendering approach that disentangles temporal and spatial deformations, thereby eliminating the reliance on 4D matrix computations. We extend the 3DGS rendering process to 4D, enabling the projection of temporal and spatial deformations into dynamic 2D Gaussians in ray space. Consequently, our method facilitates faster dynamic scene synthesis. Moreover, it reduces storage requirements by at least 4.5% due to our efficient presentation method. Our approach achieves an unprecedented average rendering speed of **343 FPS** at a resolution

of 1352×1014 on an **RTX 3090 GPU**, with experiments across multiple benchmarks demonstrating its competitive performance in both monocular and multi-view scenarios.

1. Introduction

Reconstructing dynamic scenes from 2D images and synthesizing photo-realistic novel views in real-time, has been a long-standing goal in computer vision and graphics. This task has attracted increasing attention from both academia and industry because of its potential value in various applications, including film, gaming, and VR/AR. Recently, such as NeRF [17], have achieved photo-realistic static scene rendering. However NeRF based methods typically can not support real-time rendering even for static scenes, due to their dense sampling of millions of rays. Recently, 3D Gaussian Splatting (3DGS) [10] has attracted widespread attention because of its real-time rendering ability for photo-realistic images in static scene. By modeling three-dimensional scene with 3D Gaussian ellipsoids explicitly and employing fast rasterization technique, it avoids dense ray sampling and achieves true real-time rendering in static scene.

Subsequently, many efforts [6, 26, 28, 28] have attempted to apply 3DGS to dynamic scenes. All these methods based on 3DGS can be categorized into two groups.

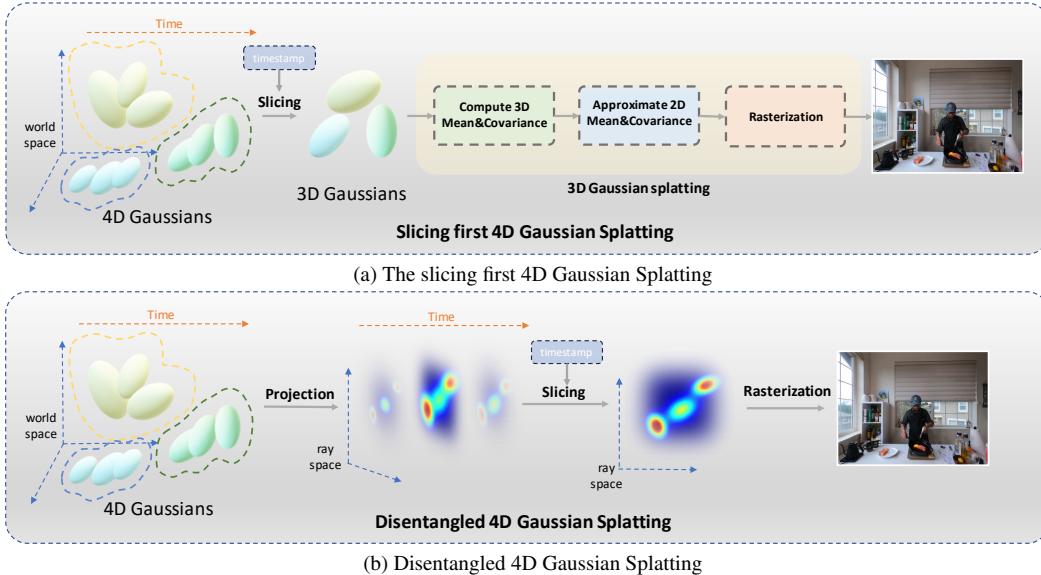


Figure 2. Comparison between Slicing first 4D Gaussian Splatting and our Disentangled 4D Gaussian Splatting. The upper one is the slicing first 4D Gaussian Splatting method, which need to slicing the 4D Gaussian into 3D Gaussian, not only do they need to calculate four-dimensional matrices, but they also have to repeat slicing and projection operations. In contrast, our method preserves temporal information during the rendering process while more conveniently obtaining continuous images in the temporal dimension.

The first group [26, 28] employs deep learning to implicitly model temporal changes in 3D Gaussian ellipsoids. To synthesize novel views of dynamic scenes, the deep learning model predicts modifications to the base 3D Gaussian ellipsoids, which are then adjusted to reconstruct the scene at a given timestamp. This updated scene is subsequently processed through the 3DGS rendering pipeline [10], where 3D Gaussian ellipsoids are projected into 2D Gaussian ellipses in ray space and efficiently rasterized to produce the final novel view image. However, since each Gaussian ellipsoid requires querying a deep learning model, these methods often struggle to achieve real-time rendering speeds for complex scenes. The second group [6, 28] extends 3D Gaussian ellipsoids into 4D Gaussian hyperspheres, modeling dynamic scenes using four-dimensional transformations, including rotation, scaling, and mean. As Fig.2a shown, to generate novel views at specific timestamps, these methods first slice the 4D Gaussian hypersphere into a 3D Gaussian ellipsoid corresponding to the given timestamp before proceeding with the 3DGS rendering pipeline. Despite their differences, both groups require transforming dynamic scenes into static representations before rendering. While this method suffices for static novel view synthesis, it is inadequate for dynamic scenes where timestamps change more frequently than viewpoints. In deep learning-based methods, temporal deformations are modeled implicitly, making direct projective transformation infeasible. Similarly, prior rotation and scaling based 4D Gaussian approaches embed temporal transformations within the four-

dimensional covariance matrix, making direct projection computationally expensive and complex. Consequently, these methods must recompute the entire rendering process whenever the timestamp changes, leading to significant redundant calculations.

To reduce redundant computations, we propose **Disentangled 4D Gaussian Splatting (Disentangled4DGS)**, an approach that differs from traditional rotation and scale based representation methods. Specifically, we represent 4D Gaussians using a combination of 3D Gaussian parameters, time scaling, and the velocity of the mean. Our method effectively disentangles the time-dependent components of the four-dimensional Gaussian sphere from other parameters, enabling projection into ray space without extensive and complex calculations. Compared to traditional methods that require incorporating a four-dimensional covariance matrix during slicing to obtain a three-dimensional Gaussian sphere for projection and rasterization as Fig.2a shown, operates directly on the projected 2D Gaussian when the timestamp changes as Fig.2b shown, thus avoiding the repetition of the process from 4D Gaussian to 2D Gaussian. Additionally, because our method requires computing only the covariance matrix of the three-dimensional Gaussian sphere rather than a four-dimensional matrix during rendering, it offers substantial computational speed advantages. Furthermore, since our representation method utilizes fewer numerical values than traditional approaches, it naturally reduces storage requirements by at least 4.5% compared to the rotation-plus-scaling method. We also provide a formal

proof of equivalence between the two representations in the **supplementary material**. Therefore, prior scene representations can be transformed into our format, enabling faster rendering using our optimized process.

The nature of Gaussian functions can lead to artifacts when expressing high-frequency information [30]. However, high-frequency features are prevalent in both spatial (e.g. sharp objects) and temporal (e.g. sudden appearance or disappearance) dimensions. And to alleviate this artifact problem that may arise from spatial high-frequency parts, we adopted an edge loss based on Laplacian convolution kernel [25] which is widely utilized to extract high-frequency parts. Experimental results indicate that our loss function significantly resolves artifact issues, enhancing rendering quality.

In complex scenarios, frequency distribution differences between time and space domains often render a unified density control strategy unsuitable. To address this, we decouple the traditional density control into temporal splitting strategy and spatial domain splitting strategy. Our approach delivers improved performance in dynamic scenes, as demonstrated by experimental results.

In summary, the key contributions of Disentangled4DGS are:

- We propose a disentangled representation for 4D Gaussians that separates time-dependent components from other parameters, eliminating the need for four-dimensional matrix operations. This approach reduces storage consumption by **4.5%** compared to traditional methods while maintaining compatibility with existing representations through transformation.
- We introduce a novel rendering pipeline for 4D Gaussians that postpones the slicing process, effectively minimizing redundant computations in dynamic scene rendering.
- We propose an edge loss based on a Laplacian convolution kernel and a temporal splitting strategy to reduce visual artifacts.
- Disentangled4DGS achieves unprecedented rendering performance, generating 1353×1014 resolution videos at an average of **343 FPS** on an RTX 3090 in Plenoptic Video Dataset [14], as shown in Fig.1. Both quantitative and qualitative evaluations demonstrate its superiority over previous methods, setting new benchmarks in rendering quality and speed.

2. Related work

2.1. Novel view synthesis for static scenes

In recent years, novel view synthesis has received widespread attention. Prior work formalized concepts like lumigraph [3] or light-field [12] and generating novel-view images through interpolating the existing views. Although traditional methods are efficient, they require densely cap-

tured images in complex scenes. Ben et al. [18] initiated a significant trend by utilizing a Multi-Layer Perceptron (MLP) to learn the radiance field and applying volumetric rendering for photo-realistic image synthesis from any viewpoint. Subsequent efforts have aimed to accelerate training and rendering [5, 19, 29] and enhance rendering quality by addressing existing issues in the NeRF [18], such as aliasing and reflection. However, NeRF [18] based methods involve querying the MLP for hundreds of points per ray, significantly consuming time. In contrast, Kerbl et al.'s 3D Gaussian Splatting (3DGS) [10] offers a novel framework enabling real-time, high-fidelity novel view synthesis for complex scenes. Recent advancements [30] have focused on enhancing both rendering speed and the quality of synthesized images.

2.2. Novel view synthesis for dynamic scenes

Unlike static scenes, novel view synthesis for dynamic scenes necessitates accurate modeling of geometric shapes and colors, as well as their temporal changes. Inspired by NeRF's success with static scenes, some works [19, 20] have attempted to extend NeRF [18] for dynamic environments, focusing on improving volume and spatiotemporal encoding for efficient dynamic scene modeling. The real-time rendering capabilities of 3DGS for photo-realistic images have drawn widespread attention. Some research [26] focuses on modeling temporal changes in 3DGS [10] using deep learning, yielding high-quality novel view synthesis. However, since each Gaussian sphere necessitates querying the model to capture temporal changes, the rendering speed is slower than the original 3DGS.

2.3. Dynamic 3D Gaussians

There has been significant progress in extending 3DGS to dynamic scenes [6, 28]. Yang et al. [28] characterize 4D Gaussian hyperspheres by expanding the quaternions and 3D scaling vectors of 3D Gaussian spheres into dual quaternions and 4D scaling vectors, and they innovatively use four-dimensional spherical harmonics to capture temporal and spatial color variations. Duan et al. [6] employ a spatiotemporal decoupled 16-dimensional vector instead of dual quaternions to represent rotation in four-dimensional space, reducing degrees of freedom and optimization complexity. These methods render images faster than deep learning-based approaches. But all of these methods need to get a static scenes at a timestamp represented by 3DGS firstly then follow the rendering pipeline of 3DGS to get a image of novel view at the timestamp. Thus these methods have low efficiency when timestamp changes frequently, which often occurs in dynamic scenarios. In contrast, by projecting the Gaussian function in ray space firstly, we can delay the time dimension in rendering, thereby reducing duplicate calculations when time changes.

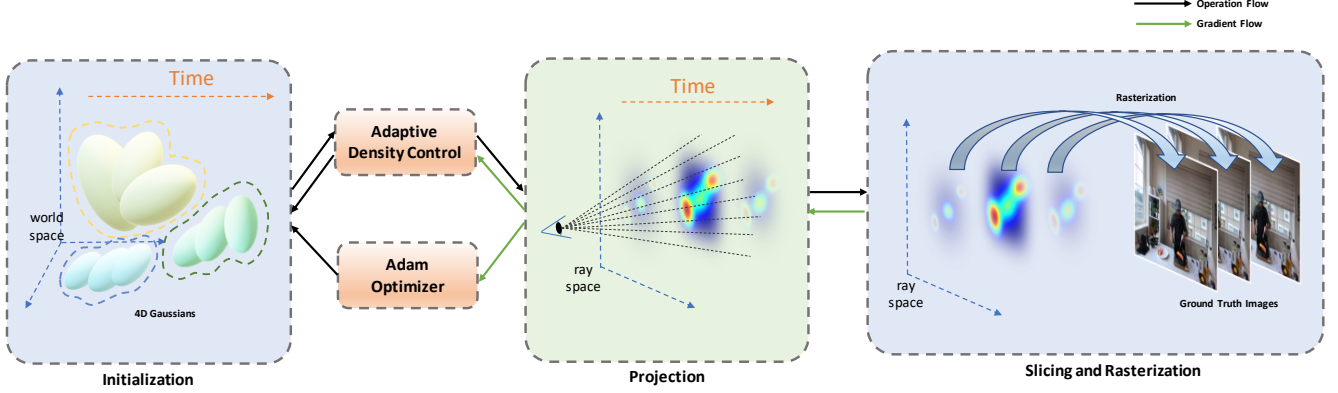


Figure 3. Rendering pipeline of our Disentangled 4DGS. After initialization, we first project the 3D Gaussians and the velocity of mean orthogonally to the timeline, obtaining a 2D Gaussian sphere with velocity in ray space. Then the projected 2D Gaussians with velocity are sliced to obtain the static 2D Gaussian in ray space and utilize rasterization to get the image in the end. The gradients from loss are back-propagated to optimize the 4D Gaussians and guide the adaptive density control

3. Method

In this section, we first review the 3D Gaussian Splatting (3DGS) method [10], which inspired our method, in Section 3.1. In Section 3.2, we detail how our method renders the novel view of dynamic scene represented by 4D Gaussian. In Section 3.3, we introduce our spatial edge loss and temporal split strategy. An overview of our framework is shown in Fig.3.

3.1. Preliminary of 3D Gaussian Splatting

3D Gaussian Splatting(3DGS) [10] has demonstrated real-time photo-realistic rendering capabilities in static scenes. It employs a set of anisotropic Gaussian ellipsoids to represent the scene. Each Gaussian ellipsoid can be characterize by a three-dimensional covariance matrix Σ and a three-dimensional mean vector μ , as described below:

$$G(x) = e^{-\frac{1}{2}(x-\mu)^T \Sigma^{-1}(x-\mu)} \quad (1)$$

To ensure that the covariance matrix Σ is positive definite and symmetric. 3DGS optimizes the scaling matrix \mathbf{S} and rotation matrix \mathbf{R} to replace direct optimizing covariance matrix. The covariance matrix Σ can be formulated by \mathbf{S} and \mathbf{R} as:

$$\Sigma = \mathbf{R} \mathbf{S} \mathbf{S}^T \mathbf{R}^T \quad (2)$$

where $\mathbf{S} = \text{diag}(s_x, s_y, s_z) \in \mathbb{R}^3$ and $\mathbf{R} \in SO(3)$ are stored as a 3D vector and quaternion. To represent the color of each Gaussian ellipsoid, 3DGS employs two sets of additional learnable parameters including opacity $o \in (0, 1)$ and spherical harmonic (SH) coefficients in \mathbb{R}^k representing the color changed by views, where k is related to SH order. The initial process of 3DGS rendering is computing the covariance matrix Σ . A view matrix then is used to transform the Gaussian ellipsoids from world space to camera space.

Because this transformation is an affine transformation, the ellipsoids are still Gaussian ellipsoids. To get the 2D reconstruction kernel in ray space [32], we need to perform a mapping $x = \phi(\mathbf{P}_{3D})$ on Gaussian ellipsoids, which can be formulated as:

$$\begin{pmatrix} x_0 \\ y_0 \\ z_0 \end{pmatrix} = \phi(\mathbf{P}_{3D}) = \begin{pmatrix} P_0/P_2 \\ P_1/P_2 \\ \|(P_0, P_1, P_2)^T\| \end{pmatrix} \quad (3)$$

where \mathbf{P}_{3D} is the coordinate in camera space and x is the coordinate in ray space. To maintain affine transformation properties, ensuring that Gaussian properties are unaltered [32], 3DGS applies the the first two terms of the Taylor expansion of ϕ to approximation, which can be defined as:

$$\phi_k(\mathbf{t}) = \mathbf{x}_k + \mathbf{J}_k(\mathbf{P} - \mathbf{P}_k) \quad (4)$$

where \mathbf{J}_k is the Jacobian matrix of ϕ at the point \mathbf{t}_k , which can be described as:

$$\mathbf{J}_k = \frac{\partial \phi}{\partial \mathbf{t}}(\mathbf{P}_k) = \begin{pmatrix} 1/P_{k,2} & 0 & -P_{k,0}/P_{k,2}^2 \\ 0 & 1/P_{k,2} & -k_{k,1}/P_{k,2}^2 \\ P_{k,0}/l' & P_{k,1}/l' & P_{k,2}/l' \end{pmatrix} \quad (5)$$

where $l' = \|(P_{k,0}, P_{k,1}, P_{k,2})^T\|$. In the end, the color of each pixel in the image is calculated by blending Gaussians sorted by their depths:

$$C = \sum_{i=1}^N c_i \alpha_i \prod_{j=i}^{i-1} (1 - \alpha_j) \quad (6)$$

where N is the number of Gaussians which influence the pixel, c_i is the color of i -th Gaussian, $\alpha_i = o_i G'_i$. For more details, please refer to [10, 32].

3.2. Disentangled 4D Gaussian Splatting

We now discuss our **Disentangled 4D Gaussian Splatting (Disentangled4DGS)** algorithm, as illustrated in Fig. 3. Specifically, we model the 4D Gaussian using 3D Gaussian (Sec. 3.2.1), time scaling and velocity of mean, and project the 4D Gaussian into ray space [32] (Sec. 3.2.2). We then slice the Gaussian in ray space and apply the fast rasterization technique to generate image.

3.2.1. Representation of 4D Gaussian

Previous works represent the 4D Gaussian hypersphere using a covariance matrix Σ_{4D} and a mean vector $\mu_{4D} = (\mu_x, \mu_y, \mu_z, \mu_t)$ to character the shape and position. To ensure that Σ_{4D} remains a positive definite symmetric matrix, they incorporate 4D rotation \mathbf{R}_{4D} and 4D scaling \mathbf{S}_{4D} into Σ_{4D} as follows:

$$\Sigma_{4D} = \mathbf{R}_{4D} \mathbf{S}_{4D} \mathbf{S}_{4D}^T \mathbf{R}_{4D}^T = \begin{pmatrix} \mathbf{U} & \mathbf{V} \\ \mathbf{V}^T & \mathbf{W} \end{pmatrix}. \quad (7)$$

Extending the 3D scaling matrix to 4D is straightforward; however, extending quaternion-based 3D rotation to 4D is more complex. Yang et al. [28] employs the dual quaternion and Duan et al. [6] adopt the 4D rotor to characterize the 4D rotations. Both of their slicing methods are based on conditional probability derivations, formulated as:

$$G_{3D}(\mathbf{x}, t) = e^{-\frac{1}{2}\lambda(x-\mu_t)^2} e^{-\frac{1}{2}[\mathbf{t}-\mu(t)]^T \Sigma_{3D}^{-1}[\mathbf{x}-\mu(t)]}, \quad (8)$$

where

$$\begin{aligned} \lambda &= \mathbf{W}^{-1}, \\ \Sigma_{3D} &= \mathbf{A}^{-1} = \mathbf{U} - \frac{\mathbf{V}\mathbf{V}^T}{\mathbf{W}}, \\ \mu_{3D} &= (\mu_x, \mu_y, \mu_z)^T + (t - \mu_t) \frac{\mathbf{V}}{\mathbf{W}}. \end{aligned} \quad (9)$$

As shown in Eq. 9, μ_{3D} is influenced by the 4D covariance matrix Σ_{4D} along the time dimension. Directly projecting the coupled scale \mathbf{S}_{4D} and rotation \mathbf{R}_{4D} is both difficult and computationally expensive. To address this, we decompose Eq. 9 into:

- **velocity of mean** $\mathcal{V}_{3D} = \frac{\mathbf{V}}{\mathbf{W}}$
- **3D Gaussian representation**, where $\mathbf{U} - \frac{\mathbf{V}\mathbf{V}^T}{\mathbf{W}}$ serves as covariance matrix Σ_{3D} , and $(\mu_x, \mu_y, \mu_z)^T$ serves as the mean vector μ_{3d}
- **Temporal scaling**, $S_t = \sqrt{\mathbf{W}}$ to ensure the variance remains positive

A detailed proof demonstrating the equivalence of these two representations is provided in the **supplementary material**. Using our representation, only the velocity of mean and temporal scaling are affected by deformations along the time dimension. Due to the projection direction is perpendicular to the time dimension to ensure that the length of

time dimension is not affected. The temporal scale S_t is unaffected by projection, while the velocity of mean \mathcal{V}_{3D} , can be easily projected similarly to the mean vector μ_{3d} .

In summary, we presentation 4D Gaussian with:

$$\begin{aligned} \mathbf{s}_{4D} &= \{\mathbf{s}_x, \mathbf{s}_y, \mathbf{s}_z, \mathbf{s}_t\}, \\ \mu_{4D} &= \{\mu_x, \mu_y, \mu_z, \mu_t\}, \\ q &= \{q_1, q_2, q_3, q_4\}, \\ \mathcal{V}_{3D} &= \{v_x, v_y, v_z\}, \end{aligned} \quad (10)$$

where \mathbf{s}_{4D} is the scaling vector, q represents the quaternion, and \mathcal{V}_{3D} denotes the velocity of mean. Our presentation effectively disentangles temporal deformations, enabling for efficient and fast projection into the ray space [32]. Compared to traditional methods requiring 16 floating-point numbers, our representation only requires 15, thereby improving storage efficiency. Consequently, our approach reduces storage requirements by at least 4.5%.

3.2.2. The Differentiable Projection First Splatting for 4D Gaussian

Following the pipeline of 3D Gaussian Splatting (3DGS), the mean of a 4D Gaussian, denoted as $\mu_{4d} = (\mu_{3d}, t)$, is transformed from world space to camera space before projection, which can be expressed as:

$$P_{3D} = \varphi(\mu_{3D}), P_t = t, \quad (11)$$

where

$$\varphi(\mu) = \mathbf{W}_{view} \mu + d_{view}. \quad (12)$$

The velocity of mean in camera space \mathcal{V}_{view} can be obtained as:

$$\begin{aligned} \mathcal{V}_{view} &= \varphi'(\mathcal{V}_{3D}), \\ \varphi'(\mathcal{V}) &= \mathbf{W}_{view} \mathcal{V} \end{aligned} \quad (13)$$

The projective transformation of the mean vector can be formulated as:

$$\begin{pmatrix} x_0 \\ y_0 \\ z_0 \end{pmatrix} = \phi_{3D}(\mathbf{P}_{3D}) = \begin{pmatrix} P_0/P_2 \\ P_1/P_2 \\ \|(P_0, P_1, P_2)^T\| \end{pmatrix}, t_0 = P_t \quad (14)$$

where $(x_0, y_0, z_0, t_0)^T$ represents the mean in ray space [32]. And the velocity of mean in ray space can be easily obtained as:

$$\begin{pmatrix} v_0 \\ v_1 \\ v_2 \end{pmatrix} = \phi'_{3D}(\mathcal{V}_{view}) = \begin{pmatrix} \mathcal{V}_{view_x}/P_2 \\ \mathcal{V}_{view_y}/P_2 \\ \|(\mathcal{V}_{view_x}, \mathcal{V}_{view_y}, \mathcal{V}_{view_z})^T \| \end{pmatrix}. \quad (15)$$

Following 3DGS we apply the Jacobian matrix of ϕ_{3D} , which can be formulated as:

$$\mathbf{J}_k = \frac{\partial \phi}{\partial \mathbf{t}}(\mathbf{P}_{k,t}) = \begin{pmatrix} 1/P_{k,t_2} & 0 & -P_{k,t_0}/P_{k,t_2}^2 \\ 0 & 1/P_{k,t_2} & -P_{k,t_1}/P_{k,t_2}^2 \\ P_{k,t_0}/l' & P_{k,t_1}/l' & P_{k,t_2}/l' \end{pmatrix}, \quad (16)$$

where

$$\begin{aligned}
 l' &= \|(P_{k,t_0}, P_{k,t_1}, P_{k,t_2})^T\|, \\
 P_{k,t} &= P_{3Dk} + (dt * \mathcal{V}_{view_k}) \\
 &= \begin{pmatrix} P_{k,0} + dt * v_{k,0} \\ P_{k,1} + dt * v_{k,1} \\ P_{k,2} + dt * v_{k,2} \end{pmatrix}, \\
 dt &= t_0 - t,
 \end{aligned} \tag{17}$$

$P_{k,t}$ represents the mean of the k^{th} Gaussian in ray space at timestamp t . And the covariance matrix Σ' in ray space is given as follows:

$$\Sigma' = JW_{view}\Sigma W_{view}^T J^T. \tag{18}$$

Then we utilize the fast rasterization technique [10] to get the image in the end.

3.3. Spatial Edge Loss Temporal Split Strategy

Artifacts significantly affect 3DGS [30] rendering quality. Unlike static scenes, dynamic scenes present both spatial and temporal artifact issues. To address the artifact problem in temporal and spatial, we utilize spatial edge loss and temporal split strategy to relieve this. Spatially, we have noticed that artifacts can lead to the abnormal of high-frequency components in image. Therefore we utilize the Laplacian convolution to obtain high frequency part and calculate L1 loss specifically for high-frequency components. It can be defined as:

$$L_{edge} = Loss_{l1}(image_L^{gt}, image_L^{render}) \tag{19}$$

where $image_L^{gt}, image_L^{render}$ denote ground truth and rendered images post-Laplacian convolution. Our total loss can be formulated as:

$$L = (1 - \lambda_1)L_1 + \lambda_1 L_{ssim} + \lambda_2 L_{edge} \tag{20}$$

Temporally, to handle the inconsistencies in the spatiotemporal frequency domain and avoid the overconfidence in time dimension we decouple the traditional splitting strategy based on xyz coordinate gradient threshold into two strategies: time-domain splitting and spatial splitting. And the time-domain splitting based on the t coordinate gradient, spatial splitting based on the xyz coordinate gradient. The spatial and temporal scale of 4D Gaussians also split separately.

4. Experiments

4.1. Datasets

In this section, we evaluate our method on two commonly used datasets, Plenoptic Video Dataset [14] and D-NeRF dataset [20], representative of various challenges in dynamic scene modeling.

Plenoptic Video Dataset [14] contains real-world multi-view videos of 6 scenes, each lasting ten seconds. These scenes incorporate complex motions and materials that are reflective or transparent. Following prior work [28], we utilize the colored point cloud generated by COLMAP from the first frame of each scene. And the resolution of 1352×1014 is adopted.

D-NeRF [20] is a monocular video dataset comprising eight videos of synthetic scenes. Following prior work [28], we utilize randomly selected points, evenly distributed within the cubic volume defined by $[-1.2, 1.2]^3$, and set their initial mean as the time duration of scene.

4.2. Implementation Details

The densification gradient threshold is set as $5e - 5$ in D-NeRF and $2e - 5$ in Plenoptic datasets. The rotors are initialized with $(1,0,0,0)$ equivalent of static identity transformation. Learning rates, densification, pruning, and opacity reset settings all follow [10]. Optimizer is Adam following prior work. For each scene we train for 20,000 steps. The LPIPS [31] in the Plenoptic Video dataset and the D-NeRF dataset are computed using AlexNet [11] and VGGNet [21], respectively.

4.3. Results of Dynamic Novel View Synthesis

4.3.1. Results on the multi-view real scenes

As detailed in Tab.1, our approach not only significantly surpasses previous methods in terms of rendering quality but also achieves substantial speed improvements. Our method renders high-resolution videos (1352×1014) at 343 FPS on an NVIDIA RTX 3090 GPU, which markedly outperforms NeRF based method. And our method also outperforms the slicing first 4D Gaussian [6, 26, 28] on rendering speed and quality. We believe our improvements over [28] mainly come from the new presentation and rendering process we proposed. As Fig.3 illustrated,

4.3.2. Results on the monocular synthetic videos

Monocular video novel view synthesis for dynamic scene is particularly challenging due to its sparse input views[6]. As summarized in Tab.2, Wu et al. [26] achieves the highest PSNR due to its directly racking 3D Gaussian deformation, which perfectly aligns with D-NeRF dataset but can not handle sudden appearances or disappearances very well. Our method achieves the fastest rendering speed among all the methods, and obtain a balanced quality. And our method can handle all kinds of scenes well, unlike [6, 27] may not perform stably in certain scenarios, such as *Lego* scene. The PSNR of Deformable3DGS [27] and Rotor4DGS [6] are 25.38, 24.93 respectively which are far away from their mean. And in contrast our method is 26.60. The variance of PSNR also demonstrates the stability of our method. The

Method	PSNR \uparrow	DSSIM \downarrow	LPIPS \downarrow	FPS \uparrow
-Plenoptic Video(real,multi-view)				
Neural Volumes*[15]	22.80	0.062	0.295	-
LLFF*[16]	23.24	0.076	0.235	-
DyNeRF*[14]	29.58	0.020	0.099	0.015
HexPlane[4]	31.70	0.014	0.075	0.056
K-Planes-explicit[8]	30.88	0.020	-	0.23
K-Planes-hybrid[8]	31.63	0.018	-	-
Mix Voxels-L[23]	30.80	0.020	0.126	16.7
StreamRF*[13]	29.58	-	-	8.3
NeRFPlayer[22]	30.69	0.035	0.111	0.045
HyperReel[1]	31.10	0.037	0.096	2.00
Deformable4DGS**[26]	31.02	0.030	0.150	36
RealTime4DGS[28]	32.01	0.014	0.16	72.80
Rotor4DGS[6]	31.62	-	0.14	277.47
Ours	32.75	0.011	0.095	342.7

Table 1. Comparison with the state-of-the-art methods on the Plenoptic Video benchmark. *:Only tested on the scene *Flame Salmon*. **:Results on *Spinach,Beef,and Steak* scenes.

Method	PSNR \uparrow	SSIM \uparrow	LPIPS \downarrow	FPS \uparrow	Variance of PSNR \downarrow
-D-NeRF (synthetic,monocular)					
T-NeRF[20]	29.51	0.95	0.08	-	-
D-NeRF[20]	29.67	0.95	0.07	-	33.23
TiNeuVox[7]	32.67	0.97	0.04	1.60	19.46
HexPlanes[4]	31.04	0.97	-	-	-
K-Planes-explicit[8]	31.05	0.97	-	-	25.37
K-Planes-hybrid[8]	31.61	0.97	0.02	-	-
V4D[9]	33.72	0.98	0.03	2.08	-
Deformable3DGS[27]	39.31	0.99	0.01	85.45	34.09
RealTime4DGS[28]	32.71	0.97	0.03	289.07	20.80
Rotor4DGS[6]	34.26	0.97	0.03	1257.63	25.48
Ours	33.34	0.97	0.03	1549.03	14.76

Table 2. Evaluation on D-NeRF Dataset

PSNR performance of each scene is shown in **supplementary material**.

4.3.3. Speed Result of Same Rendering Condition

Method	Time(ms)
Rotor4DGS[6]	0.94
Ours	0.69

Table 3. Comparison of 100,000 Gaussians CUDA rendering time

To demonstrate the excellent speed advantage of our method, we test the CUDA rendering time of the traditional 4D Gaussian methods and our method under the same view-

ing angle and the number of Gaussians is 100,000. The result in Tab. 3 shows that our rendering speed has improved by approximately 26% compared to traditional methods.

4.4. Ablation and Analysis

Tab.4 and Fig.4 ablates the effectiveness of individual designs in our method.

4.4.1. Spatial Edge Loss

As Tab.4 (c) shown, adding spatial edge loss can improve the rendering quality both in PSNR and SSIM. The effect of spatial edge loss is clearly revealed in Fig.4. For example, the detail edge around the scene *Lego, Bouncing Balls* and *T-Rex* is more refined. The burrs caused by artifacts are significant reduced. This demonstrates that the spatial

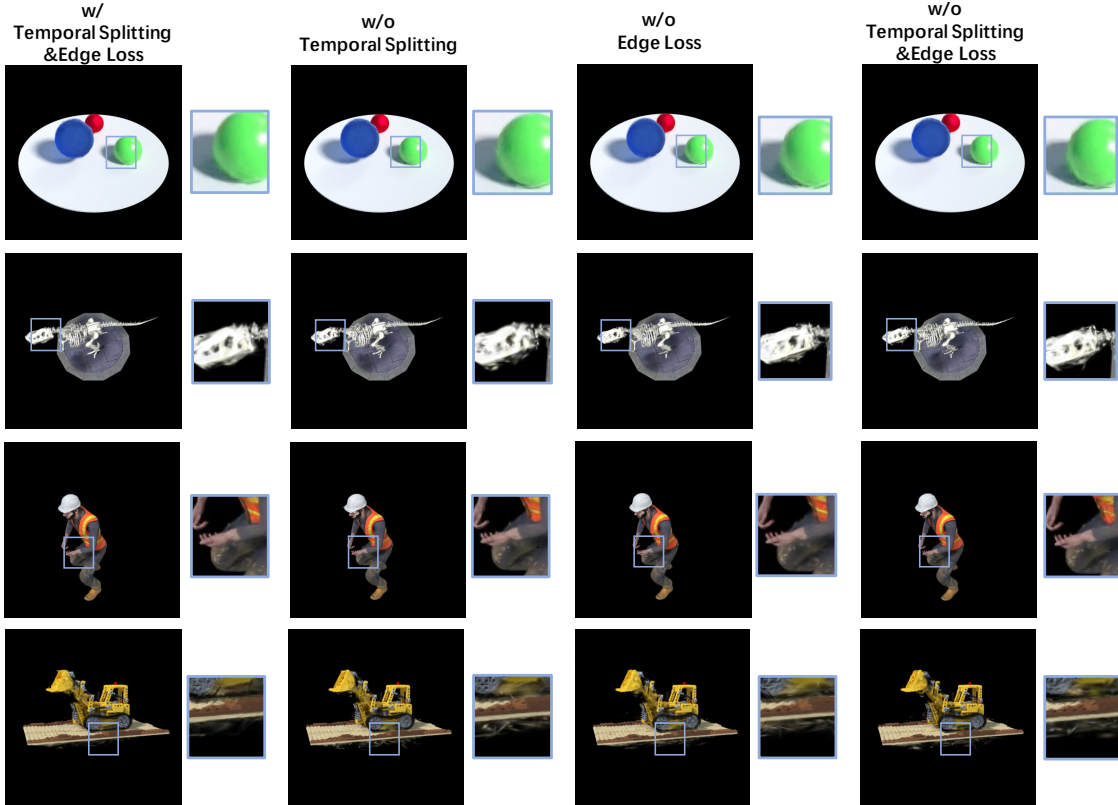


Figure 4. Comparison of rendering with and without spatial edge loss and time splitting strategy

ID	Ablation Items		D-NeRF	
	Edge Loss	Temporal Split	PSNR \uparrow	SSIM \uparrow
a			32.89	0.95
b		✓	33.07	0.96
c	✓		33.20	0.96
Full	✓	✓	33.34	0.97

Table 4. Ablation on D-NeRF Dataset. We validate two designs on rendering quality

edge loss helps reduce the artifacts and improve the expression details. Therefore, our method can handle the complex scenes better like *Lego* in D-NeRF and Plenoptic Video Dataset.

4.4.2. Temporal Splitting strategy

As shown in Tab.4 (b), our temporal split strategy can improve the quality of rendering of dynamic scenes. The over-reconstruction regions in spatial and temporal has been reduced after we decoupled the classic density control strategy. And working with spatial edge loss can significantly alleviate the artifact problem in 4D Gaussian rendering. As Fig.4 shown, the edge of the moving parts become sharper, such as jaw of *T-Rex*, edge of *Bouncing Balls* and *Lego*, cuff

in *Standup* scene.

5. Conclusion

We introduce a novel representation of 4D Gaussians that disentangles deformation within a rendering framework designed to synthesize novel views of dynamic scenes, improving compatibility with dynamic rendering scenarios. Our central approach delays the incorporation of timestamps in rendering and eliminates reliance on 4D matrix computations, thereby accelerating dynamic view synthesis. Our method achieves **343 FPS** at a resolution of 1352×1014 on an RTX 3090, while maintaining high rendering quality. To mitigate artifacts caused by overconfidence in temporal and spatial dimensions, we incorporate spatial edge loss and a temporal split strategy. Experimental results across diverse scenes demonstrate the stability of our framework. Although our method reduces the number of floating-point values required to represent 4D Gaussians, an analysis of the degrees of freedom in the 4D Gaussian sphere (provided in the **supplementary material**) suggests further compression is possible. Future work may explore the application of 4D Gaussians for segmentation and dynamic scene generation.

References

- [1] Benjamin Attal, Jia-Bin Huang, Christian Richardt, Michael Zollhoefer, Johannes Kopf, Matthew O’Toole, and Changil Kim. Hyperreel: High-fidelity 6-dof video with ray-conditioned sampling. *2023 IEEE/CVF Conference on Computer Vision and Pattern Recognition (CVPR)*, pages 16610–16620, 2023. [7](#)
- [2] Benjamin Attal, Jia-Bin Huang, Christian Richardt, Michael Zollhoefer, Johannes Kopf, Matthew O’Toole, and Changil Kim. Hyperreel: High-fidelity 6-dof video with ray-conditioned sampling. In *2023 IEEE/CVF Conference on Computer Vision and Pattern Recognition (CVPR)*, pages 16610–16620, 2023. [12](#)
- [3] Chris Buehler, Michael Bosse, Leonard McMillan, Steven J. Gortler, and Michael F. Cohen. Unstructured lumigraph rendering. *Proceedings of the 28th annual conference on Computer graphics and interactive techniques*, 2001. [3](#)
- [4] Ang Cao and Justin Johnson. Hexplane: A fast representation for dynamic scenes. *2023 IEEE/CVF Conference on Computer Vision and Pattern Recognition (CVPR)*, pages 130–141, 2023. [7](#), [12](#)
- [5] Anpei Chen, Zexiang Xu, Andreas Geiger, Jingyi Yu, and Hao Su. Tensorf: Tensorial radiance fields. *ArXiv*, abs/2203.09517, 2022. [3](#)
- [6] Yuanxing Duan, Fangyin Wei, Qiyu Dai, Yuhang He, Wenzheng Chen, and Baoquan Chen. 4d-rotor gaussian splatting: Towards efficient novel view synthesis for dynamic scenes. In *International Conference on Computer Graphics and Interactive Techniques*, 2024. [1](#), [2](#), [3](#), [5](#), [6](#), [7](#), [12](#)
- [7] Jiemin Fang, Taoran Yi, Xinggang Wang, Lingxi Xie, Xiaopeng Zhang, Wenyu Liu, Matthias Nießner, and Qi Tian. Fast dynamic radiance fields with time-aware neural voxels. *SIGGRAPH Asia 2022 Conference Papers*, 2022. [7](#), [12](#)
- [8] Sara Fridovich-Keil, Giacomo Meanti, Frederik Warburg, Benjamin Recht, and Angjoo Kanazawa. K-planes: Explicit radiance fields in space, time, and appearance. *2023 IEEE/CVF Conference on Computer Vision and Pattern Recognition (CVPR)*, pages 12479–12488, 2023. [7](#), [12](#)
- [9] Wanshui Gan, Hongbin Xu, Yi Huang, Shifeng Chen, and Naoto Yokoya. V4d: Voxel for 4d novel view synthesis. *IEEE Transactions on Visualization and Computer Graphics*, 30:1579–1591, 2022. [7](#)
- [10] Bernhard Kerbl, Georgios Kopanas, Thomas Leimkuehler, and George Drettakis. 3d gaussian splatting for real-time radiance field rendering. *ACM Transactions on Graphics*, 42(4), 2023. [1](#), [2](#), [3](#), [4](#), [6](#)
- [11] Alex Krizhevsky, Ilya Sutskever, and Geoffrey E. Hinton. Imagenet classification with deep convolutional neural networks. *Communications of the ACM*, 60:84 – 90, 2012. [6](#)
- [12] Marc Levoy and Pat Hanrahan. Light field rendering. *Seminal Graphics Papers: Pushing the Boundaries, Volume 2*, 2023. [3](#)
- [13] Lingzhi Li, Zhen Shen, Zhongshu Wang, Li Shen, and Ping Tan. Streaming radiance fields for 3d video synthesis. *ArXiv*, abs/2210.14831, 2022. [7](#)
- [14] Tianye Li, Mira Slavcheva, Michael Zollhoefer, Simon Green, Christoph Lassner, Changil Kim, Tanner Schmidt, Steven Lovegrove, Michael Goesele, Richard Newcombe, and Zhaoyang Lv. Neural 3d video synthesis from multi-view video. In *2022 IEEE/CVF Conference on Computer Vision and Pattern Recognition (CVPR)*, pages 5511–5521, 2022. [1](#), [3](#), [6](#), [7](#), [12](#)
- [15] Stephen Lombardi, Tomas Simon, Jason M. Saragih, Gabriel Schwartz, Andreas M. Lehrmann, and Yaser Sheikh. Neural volumes. *ACM Transactions on Graphics (TOG)*, 38:1 – 14, 2019. [7](#)
- [16] Ben Mildenhall, Pratul P. Srinivasan, Rodrigo Ortiz Cayon, Nima Khademi Kalantari, Ravi Ramamoorthi, Ren Ng, and Abhishek Kar. Local light field fusion. *ACM Transactions on Graphics (TOG)*, 38:1 – 14, 2019. [7](#)
- [17] Ben Mildenhall, Pratul P. Srinivasan, Matthew Tancik, Jonathan T. Barron, Ravi Ramamoorthi, and Ren Ng. Nerf: Representing scenes as neural radiance fields for view synthesis. *CoRR*, abs/2003.08934, 2020. [1](#)
- [18] Ben Mildenhall, Pratul P. Srinivasan, Matthew Tancik, Jonathan T. Barron, Ravi Ramamoorthi, and Ren Ng. Nerf. *Communications of the ACM*, 65:99 – 106, 2020. [3](#)
- [19] Thomas Müller, Alex Evans, Christoph Schied, and Alexander Keller. Instant neural graphics primitives with a multiresolution hash encoding. *ACM Transactions on Graphics (TOG)*, 41:1 – 15, 2022. [3](#)
- [20] Albert Pumarola, Enric Corona, Gerard Pons-Moll, and Francesc Moreno-Noguer. D-nerf: Neural radiance fields for dynamic scenes. *2021 IEEE/CVF Conference on Computer Vision and Pattern Recognition (CVPR)*, pages 10313–10322, 2020. [3](#), [6](#), [7](#), [12](#)
- [21] Karen Simonyan and Andrew Zisserman. Very deep convolutional networks for large-scale image recognition. *CoRR*, abs/1409.1556, 2014. [6](#)
- [22] Liangchen Song, Anpei Chen, Zhong Li, Z. Chen, Lele Chen, Junsong Yuan, Yi Xu, and Andreas Geiger. Nerf-player: A streamable dynamic scene representation with decomposed neural radiance fields. *IEEE Transactions on Visualization and Computer Graphics*, 29:2732–2742, 2022. [7](#), [12](#)
- [23] Feng Wang, Sinan Tan, Xinghang Li, Zeyue Tian, and Huaping Liu. Mixed neural voxels for fast multi-view video synthesis. *2023 IEEE/CVF International Conference on Computer Vision (ICCV)*, pages 19649–19659, 2022. [7](#)
- [24] Feng Wang, Sinan Tan, Xinghang Li, Zeyue Tian, Yafei Song, and Huaping Liu. Mixed neural voxels for fast multi-view video synthesis. In *2023 IEEE/CVF International Conference on Computer Vision (ICCV)*, pages 19649–19659, 2023. [12](#)
- [25] Xin Wang. Laplacian operator-based edge detectors. *IEEE Transactions on Pattern Analysis and Machine Intelligence*, 29(5):886–890, 2007. [3](#)
- [26] Guanjun Wu, Taoran Yi, Jiemin Fang, Lingxi Xie, Xiaopeng Zhang, Wei Wei, Wenyu Liu, Qi Tian, and Xinggang Wang. 4d gaussian splatting for real-time dynamic scene rendering. *2024 IEEE/CVF Conference on Computer Vision and Pattern Recognition (CVPR)*, pages 20310–20320, 2023. [1](#), [2](#), [3](#), [6](#), [7](#), [12](#)
- [27] Ziyi Yang, Xinyu Gao, Wenming Zhou, Shaohui Jiao, Yuqing Zhang, and Xiaogang Jin. Deformable 3d gaussians

- for high-fidelity monocular dynamic scene reconstruction. *2024 IEEE/CVF Conference on Computer Vision and Pattern Recognition (CVPR)*, pages 20331–20341, 2023. [6](#), [7](#), [12](#)
- [28] Zeyu Yang, Hongye Yang, Zijie Pan, and Li Zhang. Real-time photorealistic dynamic scene representation and rendering with 4d gaussian splatting. In *International Conference on Learning Representations (ICLR)*, 2024. [1](#), [2](#), [3](#), [5](#), [6](#), [7](#), [12](#)
- [29] Alex Yu, Sara Fridovich-Keil, Matthew Tancik, Qinhong Chen, Benjamin Recht, and Angjoo Kanazawa. Plenoxels: Radiance fields without neural networks. *2022 IEEE/CVF Conference on Computer Vision and Pattern Recognition (CVPR)*, pages 5491–5500, 2021. [3](#)
- [30] Zehao Yu, Anpei Chen, Binbin Huang, Torsten Sattler, and Andreas Geiger. Mip-splatting: Alias-free 3d gaussian splatting. *2024 IEEE/CVF Conference on Computer Vision and Pattern Recognition (CVPR)*, pages 19447–19456, 2023. [3](#), [6](#)
- [31] Richard Zhang, Phillip Isola, Alexei A. Efros, Eli Shechtman, and Oliver Wang. The unreasonable effectiveness of deep features as a perceptual metric. *2018 IEEE/CVF Conference on Computer Vision and Pattern Recognition*, pages 586–595, 2018. [6](#)
- [32] M. Zwicker, H. Pfister, J. van Baar, and M. Gross. Ewa splatting. *IEEE Transactions on Visualization and Computer Graphics*, 8(3):223–238, 2002. [4](#), [5](#)

Disentangled 4D Gaussian Splatting: Towards Faster and More Efficient Dynamic Scene Rendering

Supplementary Material

6. Equivalent Proof of Representation Methods

We demonstrate the equivalence between two parameterizations of a 4D Gaussian function. The key insight is to show that their mean vectors and covariance matrices can be transformed into each other.

6.1. Parameterization 1: Rotation-Scaling-Based Method

- Mean:

$$\mu_4 = \begin{bmatrix} \mu_s \\ \mu_t \end{bmatrix}, \quad (21)$$

where $\mu_s \in \mathbb{R}^3$ is the spatial mean, and $\mu_t \in \mathbb{R}$ is the temporal mean.

- Covariance:

$$\Sigma_1 = \mathbf{R}\mathbf{S}\mathbf{S}^T\mathbf{R}^T, \quad (22)$$

where \mathbf{R} is a 4D rotation matrix (orthogonal: $\mathbf{R}^T\mathbf{R} = \mathbf{I}$), and $\mathbf{S} = \text{diag}(s_1, s_2, s_3, s_t)$ is a diagonal scaling matrix.

6.2. Parameterization 2: Disentangled Method

- Mean: $\mu_s \in \mathbb{R}^3$ (spatial mean), $\mu_t \in \mathbb{R}$ (temporal mean), and $\mathbf{v} \in \mathbb{R}^3$ represents velocity.
- Covariance: Since

$$\mathbf{x} = \mu_s + \mathbf{v}(t - \mu_t). \quad (23)$$

The spatial covariance $Cov(\mathbf{x}, \mathbf{x})$ is represented as:

$$\begin{aligned} \Sigma_2 &= Cov(\mathbf{x}, \mathbf{x}) \\ &= Cov(\mathbf{v}(t - \mu_t), \mathbf{v}(t - \mu_t)) + Cov(\mu_s, \mu_s) \\ &= \mathbf{v}Var(t)\mathbf{v}^T + \Sigma_s \\ &= \sigma_t^2\mathbf{v}\mathbf{v}^T + \Sigma_s. \end{aligned} \quad (24)$$

The spatiotemporal covariance $Cov(\mathbf{x}, t)$ can be formulated as:

$$Cov(\mathbf{x}, t) = \mathbf{v}Var(t) = \sigma^2\mathbf{v}. \quad (25)$$

Temporal covariance $Var(t)$ is given by σ_t^2 . Thus, the 4D covariance can be obtained as:

$$\Sigma_2 = \begin{bmatrix} \Sigma_s + \sigma_t^2\mathbf{v}\mathbf{v}^T & \sigma_t^2\mathbf{v} \\ \sigma_t^2\mathbf{v}^T & \sigma_t^2 \end{bmatrix}. \quad (26)$$

6.3. Equivalent Proof

We partition the four-dimensional covariance matrix Σ_1 into blocks:

$$\Sigma_1 = \begin{bmatrix} \mathbf{A} & \mathbf{b} \\ \mathbf{b}^T & c \end{bmatrix}, \quad (27)$$

where \mathbf{A} is a 3×3 matrix, \mathbf{b} is a 3×1 vector, c is a scalar. To convert the Rotation-Scaling-Based Method to Disentangled Method, we define:

$$\begin{aligned} \sigma_t^2 &= c, \\ \mathbf{v} &= \mathbf{b}/c, \\ \Sigma_s &= \mathbf{A} - \mathbf{v}\mathbf{v}^T\sigma^2 = \mathbf{A} - \mathbf{b}\mathbf{b}^T/c. \end{aligned} \quad (28)$$

Since Σ_1 is positive definite, its Schur complement is also positive definite, ensuring that Σ_2 is a valid covariance matrix. Conversely, given the block structure of Σ_2 , we can directly construct a four-dimensional covariance matrix, from which the corresponding \mathbf{R} and \mathbf{S} can be obtained through eigenvalue decomposition.

6.4. Degree of Freedom Analysis

6.4.1. Degree of Freedom of Rotation Based Method

- Rotation matrix \mathbf{R} : The degrees of freedom (DOF) are 6. A 4D rotation can be decomposed into independent 2D plane rotations, where each pair of coordinate axes defines a rotation plane. The total number of possible rotation planes is given by the combination formula: $C(4, 2) = 6$ (planes: xy, xz, xw, yz, yw, zw).
- Scaling matrix \mathbf{S} : The degrees of freedom correspond to the four diagonal elements, resulting in 4 DOF.
- Mean μ_4 : The degrees of freedom are 4.

6.4.2. Degree of Freedom of Disentangled Method

- 3D covariance matrix Σ_s : The degrees of freedom are 6, as the covariance matrix is symmetric.
- Temporal covariance σ_t^2 : The degree of freedom is 1.
- Velocity of 3D mean \mathbf{v} : The degrees of freedom are 3.
- Mean μ_4 : The degrees of freedom are 4.

In summary, both parameterization methods have an equal total of **14 degrees of freedom**. Notably, a 3D rotation has three degrees of freedom but requires four floating-point numbers for representation. This suggests the potential for a more efficient representation that uses only three floating-point numbers for 3D rotation or **14 floating-point numbers to represent a 4D Gaussian sphere**.

7. PSNR Performance Across Different Scenes

As shown in Tab. 5 and Tab. 6, it can be seen that our method performs well compared to other methods in various scenarios on both datasets. This result further demonstrates the strong generalization ability of our approach.

Method	Coffee Martini	Spinach	Cut Beef	Flame Salmon	Flame Steak	Sear Steak	Mean
HexPlane[4]	-	32.04	32.55	29.47	32.08	32.39	31.70
K-Planes-explicit[8]	28.74	32.19	31.93	28.71	31.80	31.89	30.88
K-Planes-hybrid[8]	29.99	32.60	31.82	30.44	32.38	32.52	31.63
Mix Voxels[24]	29.36	31.61	31.30	29.92	31.21	31.43	30.80
NeRFPlayer[22]	31.53	30.56	29.353	31.65	31.93	29.12	30.69
HyperReel[2]	28.37	32.30	32.922	28.26	32.20	32.57	31.10
RealTime4DGS[28]	28.33	32.93	33.85	29.38	34.03	33.51	32.01
Ours	29.05	34.12	34.16	29.39	35.14	34.62	32.75

Table 5. Per-scenes results on the Plenoptic Video dataset

Method	Lego	Hell Warrior	Bouncing Balls	Jumping Jacks	Stand Up	Hook	T-Rex	Mutant	Mean
D-NeRF[20]	21.76	24.70	38.87	32.56	33.63	28.95	31.45	21.41	29.17
TiNeuVox[7]	25.13	28.20	40.56	34.81	35.92	31.85	32.78	33.73	32.87
K-Planes[8]	22.73	25.38	39.71	32.53	34.26	28.61	31.44	33.88	31.07
Deformable4DGS[26]	25.31	25.31	39.29	34.65	36.80	31.79	33.12	37.63	32.99
Deformable3DGS[27]	25.38	42.06	41.33	39.21	45.74	38.04	38.55	44.16	39.31
RealTime4DGS[28]	24.29	34.67	32.85	30.44	39.11	31.77	29.82	38.75	32.71
Rotor4DGS[6]	24.93	33.52	34.75	33.40	40.79	34.24	31.77	40.66	34.26
Ours	26.60	34.75	33.62	32.55	38.30	32.07	30.75	38.06	33.34

Table 6. Per-scenes results on the D-NeRF Video dataset

8. Dynamic Visualization of Results in Plenoptic Video Dataset

To effectively illustrate the performance of our method, we dynamically visualize our experimental results on the Plenoptic Video Dataset [14] as shown in the Fig. 5. Please note that the animation results may require viewing with **Adobe Acrobat**.

(a) Cut Roasted Beef

(b) Coffee Martini

(c) Cook Spinach

(d) Flame Salmon

(e) Flame Steak

(f) Sear Steak

Figure 5. Dynamic visualization of Plenoptic Video dataset